Article

Highly Sensitive Bilirubin Biosensor Based on Photonic Crystal Fiber in Terahertz Region

Ahmed Refaat Elhelw [1] , Mahmoud Salman S. Ibrahim [2], Ahmed Nabih Zaki Rashed [3] ,
Abd El-Naser A. Mohamed [1,3], Mohamed Farhat O. Hameed [4,5,6,*] and Salah S. A. Obayya [4,7,*]

1 Department of Communication and Electronic Engineering, Higher Institute of Engineering and Technology in Arish, Arish 45511, Egypt
2 Physics Department, Faculty of Science, Arish University, Arish 45511, Egypt
3 Electronics and Electrical Communications Engineering Department, Faculty of Electronic Engineering, Menoufia University, Menouf 32951, Egypt
4 Centre for Photonics and Smart Materials, Zewail City of Science, Technology, and Innovation, October Gardens, 6th of October City, Giza 12578, Egypt
5 Nanotechnology and Nanoelectronics Engineering Program, Zewail City of Science, Technology, and Innovation, October Gardens, 6th of October City, Giza 12578, Egypt
6 Mathematics and Engineering Physics Department, Faculty of Engineering, University of Mansoura, Mansoura 35516, Egypt
7 Department of Electronics and Communications Engineering, Faculty of Engineering, University of Mansoura, Mansoura 35516, Egypt
* Correspondence: mfarahat@zewailcity.edu.eg (M.F.O.H.); sobayya@zewailcity.edu.eg (S.S.A.O.)

Abstract: An unstable bilirubin level in the human blood causes many dangerous health problems, such as jaundice, coronary artery disease, ulcerative colitis, and brain lesions. Therefore, the accurate and early detection of bilirubin concentrations in the blood is mandatory. In this work, a highly sensitive biosensor based on photonic crystal fiber (PCF) for monitoring bilirubin levels is proposed and analyzed. The sensor parameters, including relative sensitivity, effective mode area, confinement loss, and effective material loss, are calculated. The geometrical parameters are studied, and a modal analysis of the suggested sensor is carried out using the full-vectorial finite element method (FEM). The fabrication tolerance of the geometrical parameters is also studied to ensure the fabrication feasibility of the reported design. High sensitivities of 95% and 98% are obtained for the x-polarized and y-polarized modes, respectively. Furthermore, a small material loss of 0.00193 cm^{-1}, a small confinement loss of 2.03×10^{-14} dB/cm, and a large effective mode area of 0.046 mm^2 are achieved for the y-polarized mode. It is believed that the presented sensor will be helpful in health care and in the early detection of bilirubin levels in the blood.

Keywords: terahertz sensor; bilirubin levels in the blood; photonic crystal fiber; biosensor

1. Introduction

The terahertz (THz) range covers the gap between the far-infrared and microwave spectrum, which spans from 0.1 to 10 THz. Furthermore, the molecular resonance of most chemical and biological materials lies in the THz region. Therefore, the THz regime has attracted the interest of researchers all over the world for different applications, including waveguiding [1] and sensing [2,3] devices. Photonic crystals have attracted attention because of their wide range of application, including logic gates [4,5] and sensors [6–10]. Photonic crystal fiber (PCF) [11] is a new kind of optical fiber that has the advantages of single-mode guidance [12], a large degree of design freedom, and a large effective mode area. Over the last decade, PCF in the THz and IR regions has been increasingly used for chemical, gas, and biomedical sensing [13,14]; communications [15,16]; and time-domain spectroscopy [17]. The geometrical parameters of PCF sensors can be controlled to achieve a sensitivity that is higher than that of traditional optical fiber [18]. In this

context, Rahaman et al. [19] proposed a liquid sensor based on a hollow-core PCF with asymmetric rectangular air holes. The presented sensor had relative sensitivities of 91.42%, 92.55%, and 94.03% for water, acetic acid, and chloroform, respectively. Bulbul et al. [20] suggested a blood component sensor with suspended circular PCFs, with four air fragments. This sensor had relative sensitivities of 96.19% for RBC, 95.57% for WBC, 95.89% for HB, 95.01% for water, and 95.39% for plasma. Another terahertz PCF sensor for blood components with square holes was presented by Islam et al. [21], with sensitivities of 99.39%, 99.27%, 99.12%, 99.03%, and 98.79% for RBC, hemoglobin, WBC, plasma, and water, respectively. Moreover, Bulbul et al. [18] proposed a hollow-core PCF sensor for determining the kerosene ratio in petrol and diesel, with a sensitivity of 98.68–98.83% for the different kerosene–petrol mixture ratios, while a sensitivity of 98.83–98.90% was achieved for the different kerosene–diesel mixture ratios. Ramachandran et al. [22] also reported a chemical sensor based on dual steering-wheel-shaped PCFs with a large noncircular air hole. The sensor [22] showed a relative sensitivity of 94.9% for water, 95.4% for ethanol, and 95.6% for benzene. Furthermore, Jibon et al. [23] introduced a THz nicotine sensor using a square-shaped core PCF, with a cladding of circular air holes arranged in a square manner, and a relative sensitivity of 83%. Podder et al. [24] presented a THz PCF for camel milk and buffalo milk sensing, with a relative sensitivity of 94.69% for camel milk and a relative sensitivity of 94.75% for buffalo milk.

Bilirubin is a yellowish pigment found in bile, a fluid made by the liver. A high level of bilirubin in the blood (>51.3 μmol/L) can cause jaundice [25], where the skin and the whites of the eyes appear yellow. This is an indicator of hemolytic anemia, low liver activity, and gallstones [26]. However, low levels (<5.47 μmol/L) can cause coronary artery disease [27], ulcerative colitis [28], and mental disabilities [29]. It has been reported that middle- and low-income countries suffer more from serious hyperbilirubinemia and kernicterus compared to other countries in the world [30]. It has been found that kernicterus is the most common reason for growth delay in children in Egypt [31]. Additionally, neonatal jaundice has been found to be one of the main significant contributing factors to cerebral palsy in children [32]. Therefore, there is a high need for a susceptible sensor for the early detection of liver activity with a cost-effective, short-time response and a portable, compact size.

In this work, a highly sensitive THz PCF biosensor was proposed for detecting bilirubin levels in the blood. The effective index (n_{eff}), relative sensitivity (*RS*), effective mode area (A_{eff}), confinement loss (*CL*), effective material loss (*EML*), and confined power fractions (η) were studied and analyzed. The proposed sensor had a circular-sectored cladding and a rectangular-shaped core with high-resistivity silicon (HRS) as the background material. A modal analysis was carried out using the full-vectorial finite element method [33] with the COMSOL Multiphysics software package [34]. To the best of our knowledge, this is the first time that a biosensor has been designed to monitor the bilirubin concentrations in the blood in the THz region, achieving a high analyte refractive index ($\approx$3.21) and absorption coefficient ($\approx$280 cm^{-1}) with very low losses. High sensitivies of 95% and 98% were obtained for the x-polarized and y-polarized modes, respectively. Furthermore, a small material loss of 0.00213 cm^{-1}, a small confinement loss of 7.741×10^{-14} dB/cm, and a large effective mode area of 0.0483 were achieved. Furthermore, the suggested sensor can be fabricated using currently available fabrication techniques.

2. Design Considerations and Sensing Mechanism

Figure 1 shows a 2D cross-section and 3D view of the suggested sensor with a diameter of 1.959 mm. The cladding region had two symmetrical air fragments. The core region consisted of 9 × 5 identical rectangular holes with the length L_c and width W_c. A large central rectangle was used to house the blood sample with the length L_a and width W_a. The total length (*L*) and width (*W*) of the core were 780 and 650 μm, respectively. The core region was connected with the outer shell of the fiber using a column of width *h* that had rectangular air holes (to reduce the material loss) with a length of 50 μm and width of 20 μm. Recently, due to the outstanding properties of the high-resistivity silicon (HRS)

in the THz regime, it has been widely used as a background material in photonic crystal fibers [35]. The HRS material has an average high refractive index of 3.417 and an average absorption coefficient of 0.015 cm^{-1} at a frequency range from 0.5 to 1.1 THz [36]. The refractive index and absorption coefficient of the blood as a function of bilirubin concentrations from 4 to 12 μmol/L are given by the experimental measurements in [37], where the glucose concentration values were variated from 5.0 to 5.5 mmol/L to keep the blood samples at constant conditions. In these measurements, the refractive index and the absorption coefficient of the blood samples decreased as the bilirubin concentration increased. Furthermore, the human bilirubin contains 96% as nonpolar insoluble bilirubin that is attached to albumin. The remaining 4% are combined with glucuronic acid. Therefore, an increase in the bilirubin concentration accompanies an increase in the concentration of albumin, and this decreases the blood absorption coefficient. Thus, the refractive index of blood also decreases with the increase in the bilirubin concentration [37]. Moreover, THz spectroscopy determines the concentration of polar water molecules that are combined with bilirubin in the blood, which examines only the effect of the bilirubin level on the refractive index and absorption coefficient. Moreover, it has been reported that the other blood outlier factors (hemoglobin, white blood cells, and red blood cells) have no effect on the THz wave absorption and the refractive index of the whole blood at a glucose concentration range of 105.8–136.9 mg/dL (corresponding to 5.87–7.6 mmol/L) and at a frequency near 0.5 THz [38]. The glucose concentration in our study was in the same range reported in [38]. Therefore, the main factor affecting the refractive index and absorption coefficient of the whole blood is the bilirubin only.
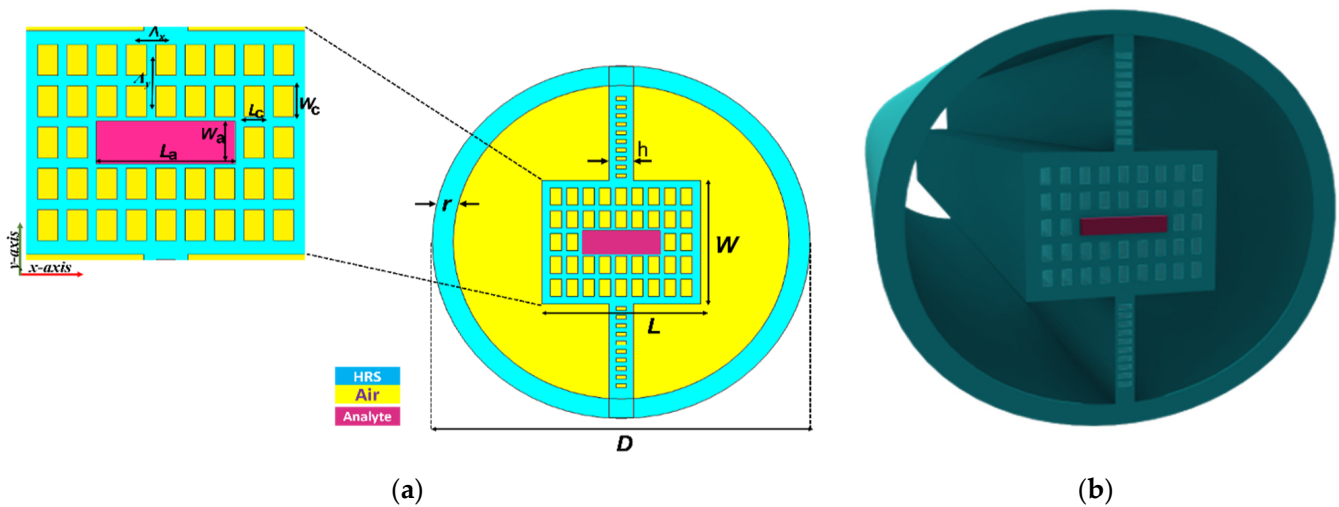

Figure 1. (**a**) 2D cross-sectional diagram; (**b**) 3D view of the suggested biosensor.

Compared to previously reported THz slot PCFs, it is believed that the fabrication of the proposed structure is possible through the conventional stack-and-draw technique [39]. It is also possible to fabricate the rectangular air hole using the extrusion technique [40]. The sample can be infiltrated within the central rectangle using the selective infiltration technique [41]. The rectangular core air holes had an initial length of L_c = 75 μm and initial width W_c = 45 μm, and they were placed in a square lattice with a lattice constant Λ_x = 80 μm in the x-direction and Λ_y = 120 μm in the y-direction. The diameter (*D*) of the cladding air fragment was equal to 1856 μm. Furthermore, the length (L_a) and the width (W_a) of the central rectangle were equal to 365 and 75 μm, respectively. In addition, the structure width (*h*) of the proposed PCF was taken as 120 μm, and the thickness of the fiber's wall (*r*) was taken as 103 μm. Table 1 shows the value of the geometrical parameter for the initial biosensor design. These initial parameters were chosen for the fabrication feasibility of the proposed design.

Table 1. The initial geometrical parameters of the proposed biosensor design.

Geometrical Parameter	Value (µm)
L_a	365
W_a	75
L_c	75
W_c	45
Λ_x	80
Λ_y	120
D	1856
R	103
H	120
L	780
W	650

Although the proposed work was based on simulations, a schematic diagram for the sensing setup is presented in Figure 2. An ultrafast femtosecond laser source was used to produce the laser beam, which was incident onto a beam splitter. Then, the two beams, called probe and pump beams, were generated [24].
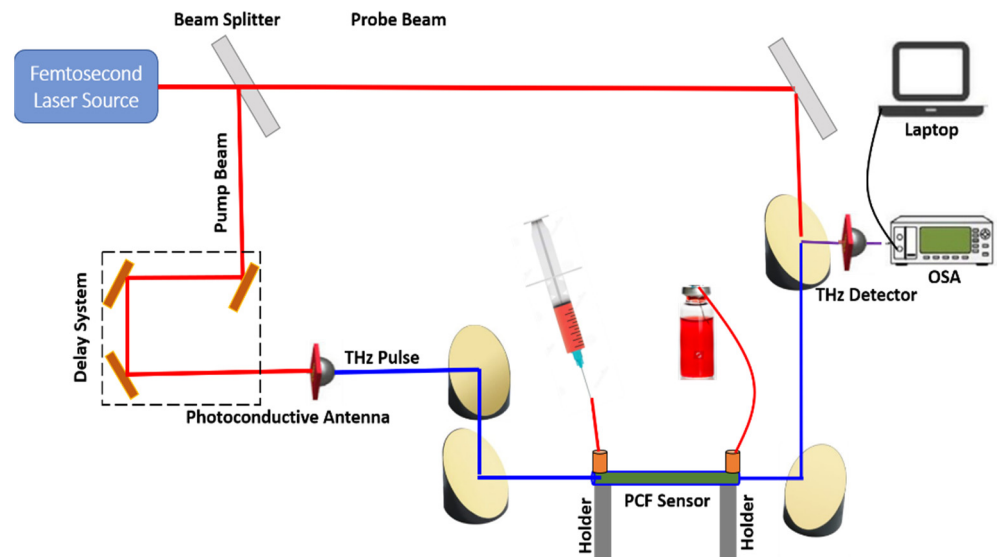

Figure 2. Schematic diagram of the experimental setup of the proposed sensor for practical sensing application.

Secondly, the pump beam was incident on a photoconductive antenna (THz emitter) to emit the THz pulse. A system of parabolic mirrors was used to align and synchronize the THz beam onto the PCF core region, where two irises were used to fix the sensor. The blood samples with different bilirubin concentrations could be selectively infiltrated inside the core region using a hypodermic syringe based on the capillary action. The syringe was used to infiltrate the analyte into the core through the face opposite to the blocked end. The solution could be slowly fed from the hypodermic syringe to ensure that the analyte sample did not enter the fiber cladding [42]. The syringe did not affect the core's refractive index, because it was removed immediately after the filling process. Injection of the UV-cured polymer was used to block the cladding holes and keep the central core hole open [43]. In addition, femtosecond laser micromachining could be used to block all the air holes using a section of conventional single mode fiber. Then, femtosecond laser direct drilling was used to open the selected holes through the blocked end [43]. In addition, the cladding holes could be blocked by selective sealing with molten uncured polymer. Then, analyte was infiltrated into the unsealed holes via capillary effects [44]. The transmitted THz beam could be realigned and refocused onto the photoconductive

THz detector. The probe beam met the detector to measure the incident electric field with amplitude attenuation and time delay based on the THz pulse absorption of bilirubin. A delay unit was used to offset the pump and probe pulses and helped in the THz temporal analysis. A Fourier transform was then used to convert the time-domain spectroscopy into a frequency domain spectrum. The blood refractive index variation modulated the intensity of the transmitted optical power. The intensity modulation could be analyzed by the optical spectrum analyzer (OSA), and the output could be investigated using the computer to obtain the performance parameters, such as sensitivity and *CL*. The computer represented the data both numerically and graphically. The cutback method and external lenses were used to eliminate the coupling loss that resulted from the lateral misalignment of the system [45]. Currently, modern technologies overcome the THz gap in the sources, detectors, and coupling devices by developing an efficient device [46].

3. Numerical Results and Discussion

The modal characteristics of the supported x- and y-polarized modes were studied using the full vectorial finite element method (FEM) [47,48]. A numerical analysis was performed using COMSOL Multiphysics software, with a minimum element size of 0.1 μm, a maximum triangular element size of 20 μm, and an element growth rate of 1.1. Furthermore, the curvature factor was fixed at 0.2. Hence, the number of degrees of freedom was 241,055, and the obtained error from the convergence study was of the order 10^{-21}. Moreover, a circular scattering boundary condition was used to absorb the outgoing waves. The fundamental mode electric field distributions for the two polarized modes using the initial parameters are shown in Figure 3, at 0.75 THz. It was revealed that the field intensity was maximum at the central region, with good confinement within the analyte core region for both polarization modes. Hence, a good light-analyte interaction could be achieved. It was also evident from Figure 3 that the confinement through the core region decreased by increasing the bilirubin concentrations. This was due to the refractive index of the blood decreasing as the bilirubin concentration increased. Therefore, the contrast in the refractive index between the cladding and core regions decreased. Subsequently, the mode field tried to dissipate towards the cladding.
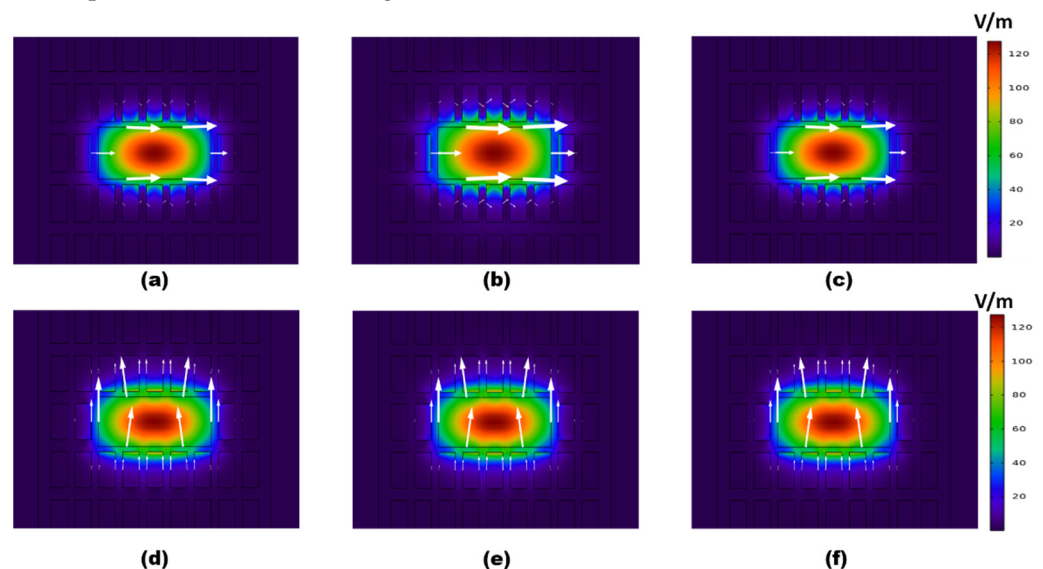
Figure 3. The electric field distribution of the fundamental mode for the (**a**–**c**) x-polarized mode and the (**d**–**f**) y-polarized mode at *f* = 0.75 THz, C = 4, 8, and 12 μmol/L, respectively. The initial dimensions shown in Table 1 are used.

Figure 4 shows the variation of the effective index with the frequency for both the x- and y-polarized modes at different bilirubin concentrations. It may be seen that the effective index increased as the operating frequency increased. This was due to the good

confinement of the mode through the high index core at large frequencies. Moreover, as the concentration of bilirubin increased, the refractive index of the analyte sample decreased. Therefore, the effective index of the supported modes decreased by increasing the bilirubin concentration [49]. The difference in the effective index between the x- and y-polarized modes was due to the asymmetrical structure of the core rectangular air hole [50,51].
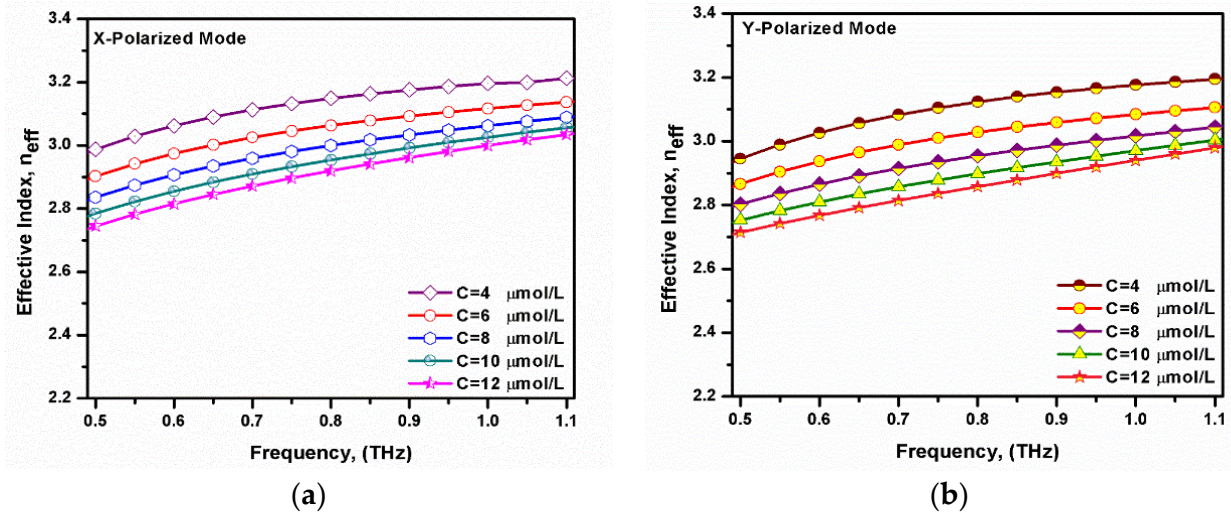
Figure 4. Variation of the frequency-dependent effective index of the fundamental (**a**) x-polarized mode and (**b**) y-polarized mode at different bilirubin concentrations.

The effective material loss (*EML*) of the PCF was a limiting factor for the sensor's performance. This loss mechanism occurred due to the absorption of the fiber background materials. Therefore, rectangular air holes were used to reduce the material loss. The *EML* can be calculated as [52–57]:

$$EML = \sqrt{\left(\frac{\varepsilon_o}{\mu_o}\right)} \left(\frac{\int_{HRS} n_{HRS} |E|^2 \alpha_{HRS} \, dA}{2 \int_{all} S_z \, dA} \right) \tag{1}$$

where *EML* is measured in cm^{-1}, ε_o is the relative permittivity, and μ_o is the relative permeability of the free space. Moreover, n_{HRS} and α_{HRS} are the refractive index and absorption coefficient of the *HRS* material, respectively, while S_z denotes the z-component of the Poynting vector. The variations in the *EML* with the frequency for the two polarized modes at different bilirubin concentrations are shown in Figure 5. As the concentration of the bilirubin increased, the refractive index of the analyte sample decreased. The refractive index range of the infiltrated analyte within the core region was 2.666–3.213, corresponding to the analyte concentration of 12–4 μmol/L. However, the refractive index of the cladding material was equal to 3.417. It should be noted that the air hole slots in the background material decreased the effective refractive index of the cladding region. Furthermore, the index difference between the core region and the cladding region decreased by increasing the analyte's concentration and, hence, the confinement of the supported modes will decrease. This will increase the interaction of the x- and y-polarized modes with the *HRS* material with increased *EML* [58], as shown in Figure 5. The proposed sensor had low *EML* values of 0.0069 cm^{-1} and 0.0065 cm^{-1} for the x- and y-polarized modes, respectively, at *f* = 0.75 THz. The obtained *EML* values were lower than those reported in [23,24].

The analyte sensing area of the PCF sensor is provided by calculating the effective mode area (*A_eff*) of the fundamental mode through the core region, as given in [18]:

$$A_{eff} = \frac{\left(\int |E^2| \, dxdy \right)^2}{\int |E^4| \, dxdy} \tag{2}$$

where *E* denotes the transverse electric field intensity. Figure 6 shows the variation in the effective mode area with the frequency at different bilirubin concentrations. It may be seen that the effective mode area decreased with the increasing operating frequency. This was due to the electric field being more confined through the analyte by increasing the frequency [59,60]. It was also noted that the effective mode area increased with a decreasing refractive index of the analyte (i.e., increasing the bilirubin concentration). For lower indexed analyte, the light confinement through the core region will be reduced [61]. The obtained effective mode areas were 0.0526 mm^2 and 0.0551 mm^2 for the x-polarized mode and y-polarized mode, respectively, at *f* = 0.75 THz.
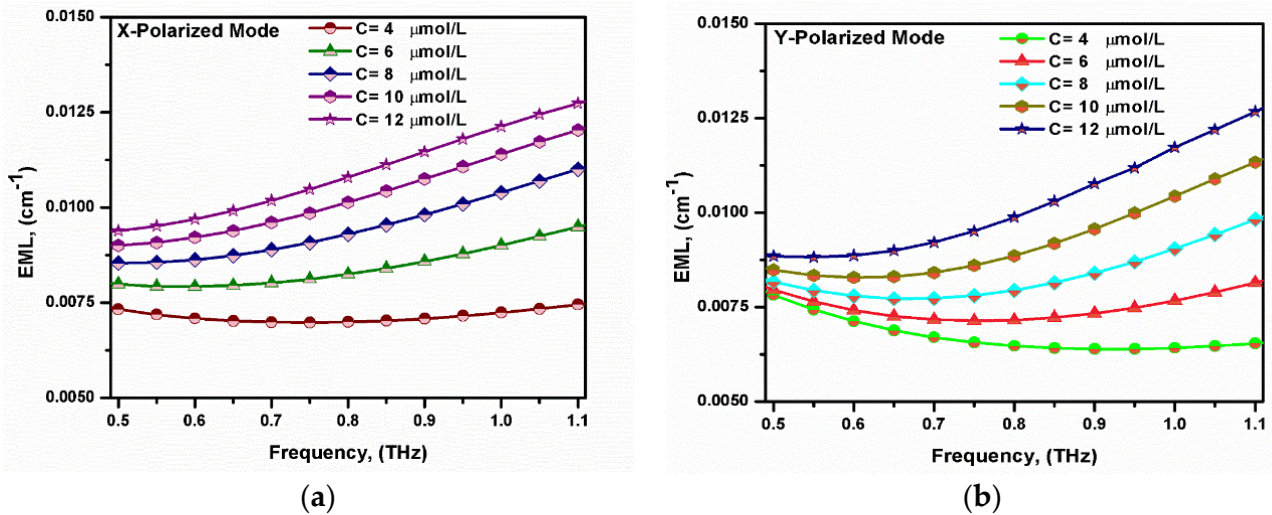

Figure 5. The variation of the EML with the frequency for the fundamental (**a**) x-polarized mode and (**b**) y-polarized mode at different bilirubin concentrations.
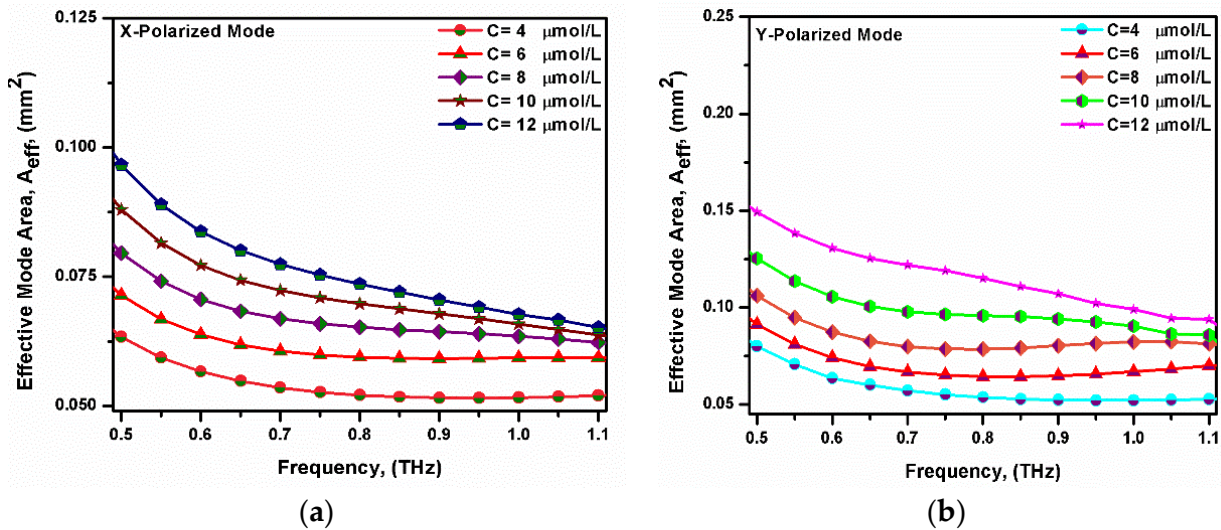
Figure 6. Variation in the effective mode area with the frequency for the fundamental (**a**) x-polarized mode and (**b**) y-polarized mode at different bilirubin concentrations.

The confinement loss (*CL*) is another loss property that affects the sensor's performance. It can be calculated using the imaginary part of the effective index as given by [62]:

$$CL = 8.686 \times \left(\frac{2\pi f}{c} \right) Im\left(n_{eff} \right) \qquad (3)$$

where f, c, and n_{eff} are the operating frequency, speed of light in a vacuum, and the effective index of the studied mode, respectively. Figure 7 shows the variation in the confinement loss of the suggested sensor with the operating frequency. It was noted that the confinement loss decreased with the increasing frequency. Moreover, the confinement loss decreased by decreasing the bilirubin concentrations. This was owing to the well confinement through the core region at higher frequencies. As the bilirubin concentration increases, the analyte refractive index will decrease. Therefore, a low index contrast between the core and cladding region occurs with reduced light confinement in the core region. The proposed sensor had very low confinement loss values of 2.05×10^{-14} dB/cm and 8.204×10^{-15} dB/cm for the x- and y-polarized modes, respectively, at f = 0.75 THz.

Figure 7. Variation in the confinement loss with the frequency for the fundamental (**a**) x-polarized mode and (**b**) y-polarized mode at different bilirubin concentrations.

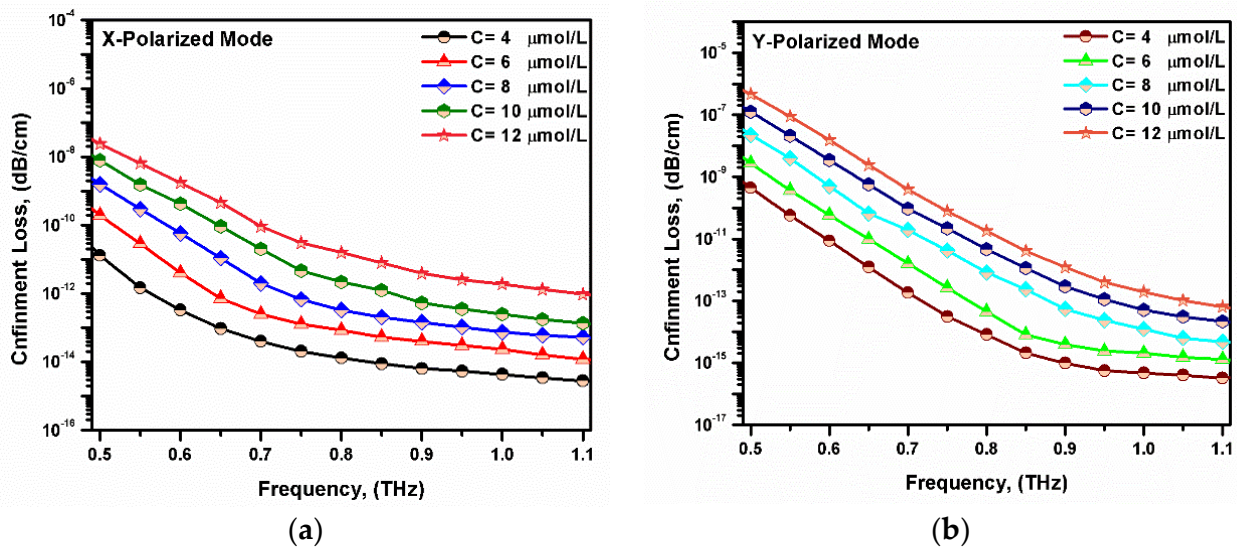The core power fraction (η) is a very important property and represents the percentage of the propagated light power inside the core region to the total power through the PCF. It can be calculated by the following equation [63]:

$$\eta = \frac{\int_{analyte} S_z \, dxdy}{\int_{all} S_z \, dxdy} \times 100 \tag{4}$$

where η is the power fraction, and S_z is the z-component of the Poynting vector. Figure 8 shows the variation in the analyte power fraction versus the frequency. It was noted that the power fraction in the analyte region increased with the increase in the operating frequency to 0.6 THz and then started to decrease. The reason behind that is the light with a higher frequency tries to propagate through the higher refractive indexed material. Therefore, some light leaks through the background material [52,64,65]. The power fraction also increased as the bilirubin concentration decreased, which increased the analyte refractive index [61]. This will increase the index contrast seen by the two polarized modes with better confinement in the core region. The maximum power fraction within the analyte region of the x- and y-polarized modes were 54.82% and 59.74%, respectively, at f = 0.75 THz.

The relative sensitivity is used to realize the sensing performance of the PCF sensor and can be calculated by the following [66]:

$$RS = \left(\frac{n_r}{n_{eff}}\right) \times \eta \tag{5}$$

where n_r is the analyte refractive index, n_{eff} is the effective mode index, and η is the analyte power fraction given by Equation (4). Figure 9 shows the variation in the relative sensitivity with the operating frequency for both the x- and y-polarized modes. It was revealed that the relative sensitivity increased with the increase in the operating frequency to 0.6 THz and then started to decrease. This can be attributed to the behavior of the core power fraction. Furthermore, the relative sensitivity of the y-polarized mode was higher than that of the x-polarized mode. Since the core had a greater geometrical dimension in the y-direction, hence, it provided a larger core power fraction [61]. The maximum sensitivity obtained for the proposed sensor was approximately 56.29% and 61.88% for the x- and y-polarized modes, respectively, at f = 0.75 THz.

Figure 8. The variation in the power fraction with the frequency for the fundamental (**a**) x-polarized mode and (**b**) y-polarized mode at different bilirubin concentrations.
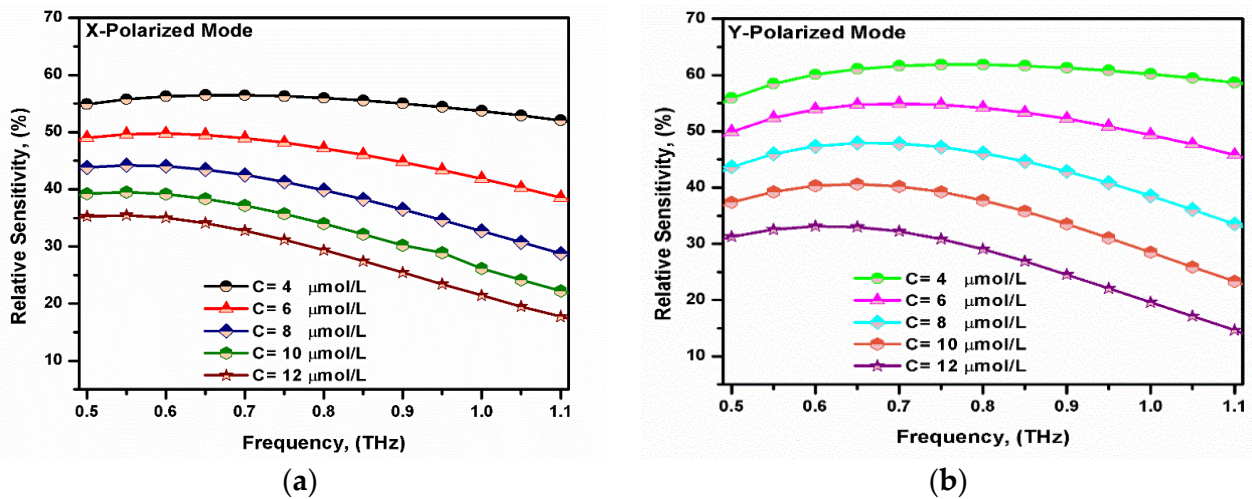
Figure 9. Variation in the relative sensitivity with the frequency for the fundamental (**a**) x-polarized mode and (**b**) y-polarized mode at different bilirubin concentrations.

In order to maximize the sensitivity of the proposed sensor, the optimization of the different geometrical parameters was performed. The variation in the relative sensitivity of both polarized modes with the core length (L_a) is first presented in Figure 10a, while the other parameters were kept constant at their initial values. However, the variation in the relative sensitivity of both polarized modes with the core width (W_a) is shown in Figure 10b

at f = 0.75 THz and C = 4 µmol/L. It is revealed from Figure 10 that the relative sensitivities of the two polarized modes increased by increasing the studied parameters. This was due to the increase in the analyte area, which increased the core power fraction [60,66]. It is also worth noting that the geometrical parameters were chosen for the ease of fabrication. Therefore, L_a = 377 µm and W_a =124 µm were chosen for the suggested design. It is also evident that the relative sensitivity of the y-polarized mode was better than that of the x-polarized mode. This was due to the core power fraction of the y-polarized mode being greater than that of the x-polarized mode [58,61].
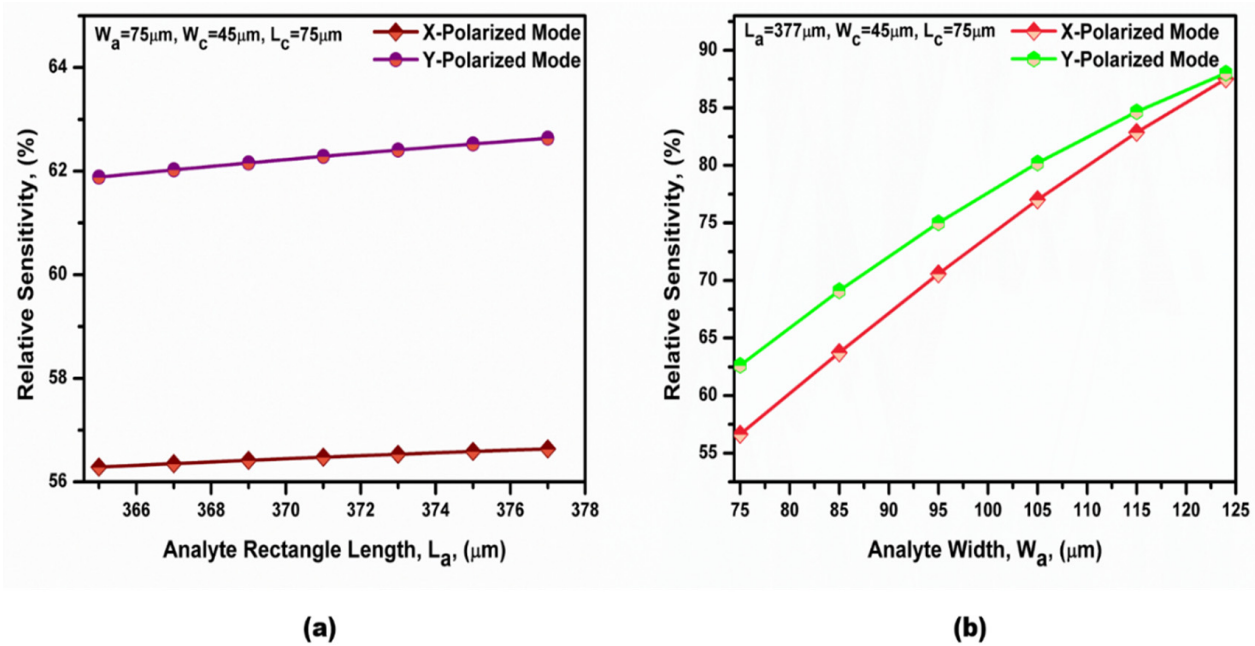
Figure 10. Dependence of the relative sensitivity on (**a**) the analyte rectangle length (L_a) and (**b**) the analyte rectangle width (W_a) at a bilirubin concentration equal to 4 µmol/L and f = 0.75 THz.

The variation in the relative sensitivity of both polarized modes with the cladding rectangular hole width (W_c) is presented in Figure 11a, at L_c = 75 µm. Furthermore, the variation in the relative sensitivity of both polarized modes with the cladding rectangular hole length (L_c) is shown in Figure 11b, at W_c = 55 µm. As the studied parameters increased, the air cladding regions increased, which increased the index contrast between the core and cladding regions. Therefore, the filed confinement of the two polarized modes in the core region increased. Hence, the relative sensitivity was increased by increasing the studied parameters, as shown in Figure 12. In the next study, W_c = 55 µm and L_c = 90 µm were taken for the subsequent simulations. A maximum relative sensitivity of 95% and 98% were obtained for the x-polarized and y-polarized modes at the optimized geometrical parameters listed in Table 2. It should be noted that during the fabrication process, the minimum distance between the holes must not be smaller than 4 µm [53,67] due to the possible fluctuations of the geometrical parameters during the fabrication process.

Table 2. The geometrical parameter values for the optimized biosensor.

Geometrical Parameter	Value (µm)
L_a	377
W_a	124
L_c	90
W_c	55
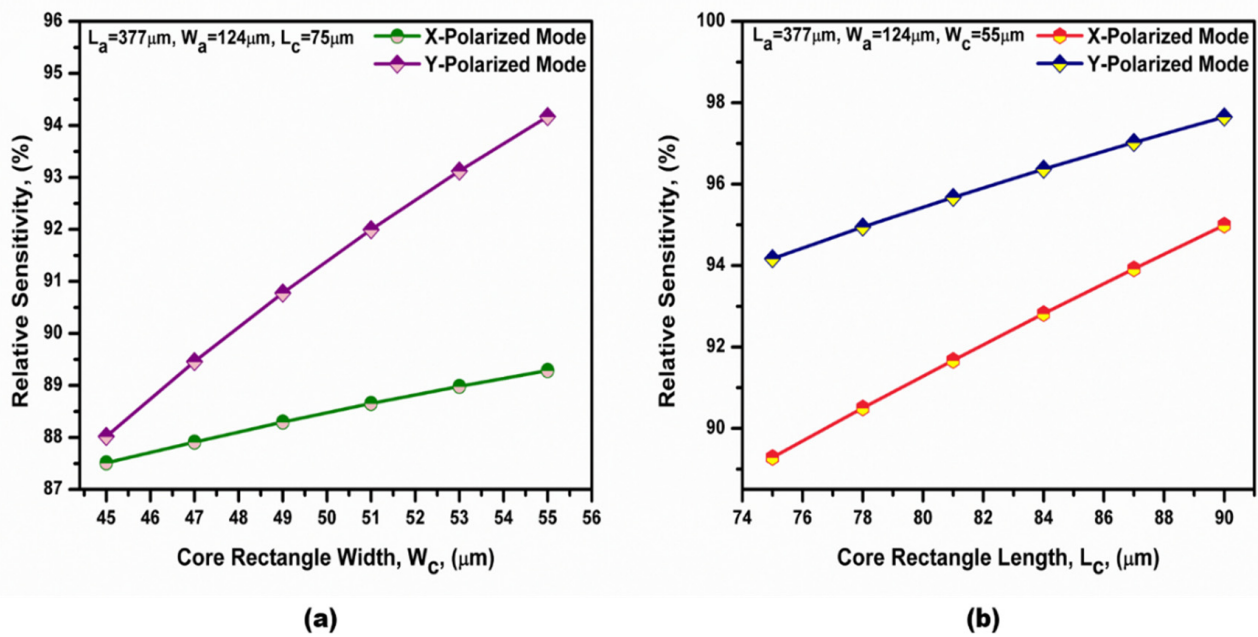
Figure 11. Dependence of the relative sensitivity on (**a**) the cladding rectangular hole width (W_c) and (**b**) the cladding rectangular hole length (L_c) at a bilirubin concentration equal to 4 μmol/L and f = 0.75 THz.
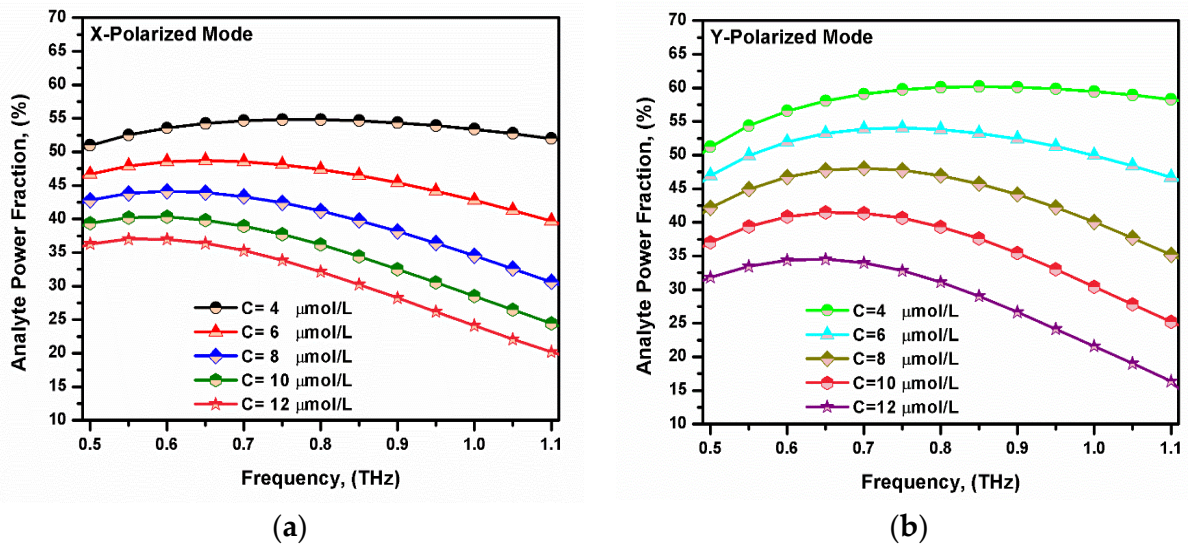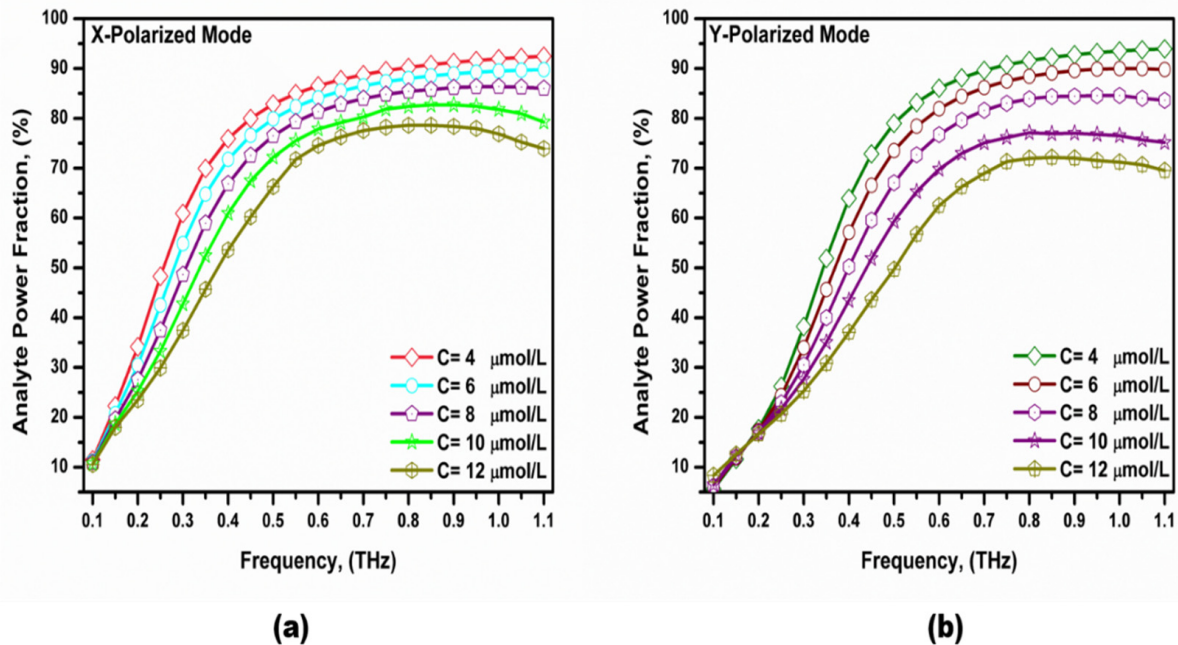

Figure 12. The variation in the analyte power fraction with the frequency for the fundamental (**a**) x-polarized mode and (**b**) y-polarized mode at different bilirubin concentrations for the optimized design.

Table 3 presents the fabrication tolerance effect on the different PCF sensor parameters to consider the fabrication faults. The effect of the analyte rectangle length (L_a) and width (W_a) and cladding rectangular air hole length (L_c) and width (W_c) were studied with a tolerance of ±2% and ±4%, relative to their optimized values at f = 0.75 THz for the y-polarized mode. It was revealed that a minimum relative sensitivity of 96.15% and a maximum value of the relative sensitivity of 98.76% was obtained within a tolerance of

−4% in the width and tolerance of +4% in the length of the analyte rectangle, which ensures the feasibility of the proposed design.

Table 3. Fabrication tolerance of the length and width of the analyte rectangle and the cladding rectangular holes of the proposed terahertz biosensor.

Parameter Variation		Sensitivity (%)	A_{eff} (mm^2)	Confinement Loss (dB/cm)	EML (cm^{-1})
L_c	+2%	98.02	0.0457	1.46×10^{-15}	0.00189
	+4%	98.36	0.0455	6.96×10^{-15}	0.00185
W_c	+2%	98.22	0.0454	6.52×10^{-15}	0.00187
	+4%	98.76	0.0421	2.22×10^{-15}	0.00182
L_a	+2%	98.19	0.0455	4.49×10^{-14}	0.00185
	+4%	98.62	0.0451	4.28×10^{-14}	0.00180
W_a	+2%	98.24	0.0461	3.58×10^{-14}	0.00181
	+4%	98.76	0.0461	8.04×10^{-14}	0.00170
Optimum		**98**	**0.0460**	**2.03×10^{-14}**	**0.00193**
L_c	−2%	97.28	0.0464	3.35×10^{-14}	0.00197
	−4%	96.90	0.0467	1.78×10^{-13}	0.00201
W_c	−2%	97.07	0.0467	5.80×10^{-14}	0.00198
	−4%	96.46	0.0474	1.03×10^{-14}	0.00204
L_a	−2%	96.98	0.0467	9.88×10^{-15}	0.00202
	−4%	96.15	0.0474	2.14×10^{-14}	0.00213
W_a	−2%	97.02	0.0460	4.57×10^{-15}	0.00205
	−4%	96.34	0.0460	3.82×10^{-15}	0.00217

Table 4 shows a comparison between the proposed design and some of those recently reported in the literature. Our sensor shows a higher sensitivity than that presented in [19,20,22–24,51,53,63–85] and is comparable with that reported in [18]. Furthermore, the suggested sensor showed lower confinement loss than that suggested in [19,63,68–70,72], and it is comparable with that proposed in [18,20,53]. In addition, the introduced sensor had a lower EML than all of those reported in Table 4. Moreover, the suggested sensor was compared with the corresponding silica-based PCF in the wavelength range of 0.8 to 2 µm [83–87]. It was revealed that the silica-based PCF sensors had low sensitivity and high confinement loss compared to the proposed sensor. Furthermore, it may be seen that the proposed sensor achieved very high sensitivity compared with silica-based PCF in the THz region, as reported in [64]. In addition, in THz region, the sensor can easily be fabricated compared to those in the optical regime. Additionally, the molecular resonances occurred in the terahertz range, making it an ideal candidate for chemical and biological sensing. Moreover, the PCF sensors worked outstandingly well, especially in the THz region, with a higher sensitivity and lower confinement loss than conventional PCF at an optical wavelength of 1.55 µm, as shown in Table 4. Considering all of the guiding and efficiency parameters, our sensor showed a remarkable performance in bilirubin sensing. Furthermore, there are different methods that have been developed for the measurement of bilirubin concentrations in medical samples. Direct spectroscopic measurement is widely used as a fast and simple method to detect bilirubin concentrations [88], but it has some drawbacks, such as the result being pH dependent [89], altered by other hemeproteins, and having low sensitivity [90]. A fluorometric biosensor is another detection method that is based on measuring the fluorescence of bilirubin [91]. It is observed that the bilirubin is very weakly fluorescent. Therefore, a special environment is needed to detect the bilirubin and enhance its emission, such as the presence of albumin bounded with bilirubin to enhance its fluorescence [92]. Highly emissive metallic nanoparticles can also be used due to the fact of their emissions being dependent on bilirubin concentrations [91]. In addition, an electrochemical biosensor can measure the oxidation potential of bilirubin into biliverdin.

The demerits of the electrochemical sensor are that oxidation reaction relies on the pH of the environment; the measurement could interfere with other biological substances, such as glucose, ascorbic acid, uric acid, and glutathione [93]; and it has a very long response time. Moreover, an optical fiber-based sensor has been developed for measuring the absorption of the bilirubin in a cuvette [94]; this method needs flat reflecting surfaces [92].

Currently, there are great developments in the field of optical sensors. Some of these sensors are based on the edge topological defect state in a 1D photonic crystal [95]. However, these sensors are not easy to fabricate due to the lattice mismatch at the interface between the two photonic crystal layers [96] and due to the fact of their very small dimensions compared to our design. Additionally, new optical sensors have been implemented based on the excitation of high wave vector modes in metamaterials [97]. However, metamaterial sensors suffer from a complicated fabrication process with expensive equipment where prism or grating coupling configurations are needed [98].

Table 4. Comparison between the guiding parameters of the suggested biosensor with the sensors in the literature. NA: Not Available.

Reference	Analyte	Background	Wavelength/Frequency	Sensitivity (%)		Confinement Loss (dB/cm)		EML (cm^{-1})	
				x-pol	*y*-pol	*x*-pol	*y*-pol	*x*-pol	*y*-pol
[18]	Adulterated diesel/petrol	Zeonex	1.5–3 THz	98.89 98.67	98.90 98.68	1.58×10^{-14} 9.50×10^{-15}	1.58×10^{-14} 9.50×10^{-15}	0.00796 0.00779	0.00796 0.00779
[19]	Water Acetic acid Chloroform	Topas	1–2 THz	91.42 92.55 94.03	91.30 92.47 93.99	1.06×10^{-9} 2.02×10^{-10} 1.39×10^{-11}	NA	NA	NA
[20]	RBC HB WBC Plasma Water	Zeonex	1–3 THz	96.17 95.54 95.87 95.37 94.97	96.18 95.57 95.89 95.39 95.01	NA	2.34×10^{-14} 4.99×10^{-15} 7.2×10^{-16} 2.15×10^{-15} 7.16×10^{-15}	0.005 0.0048 0.0049 0.0047 0.0046	0.005 0.0048 0.0049 0.0047 0.0046
[22]	Water Ethanol Benzene	Topas	1–3 THz	94.6 95.2 95.4	94.9 95.4 95.6	NA	NA	NA	NA
[23]	Nicotine	Zeonex	1–2 THz	83	83	1.00×10^{-17}	1.00×10^{-17}	0.0082	0.0082
[24]	Milk	Zeonex	1–3 THz	93.79	94.69	NA	NA	0.0064	0.0079
[51]	Air pollutants	Topas	0.6–1.2 THz	91	NA	10^{-16}	NA	0.019	NA
[63]	Sarin Soman Tabun	Zeonex	1–2 THz	90.8 91.3 92.5	91.2 91.7 92.7	1.82×10^{-12} 2.08×10^{-12} 2.73×10^{-12}	2.47×10^{-12} 2.22×10^{-12} 3.78×10^{-12}	0.00683 0.00737 0.00760	0.00687 0.00747 0.00770
[59]	Ethanol Benzene Water	Silica	1–3 THz	68.48 69.20 66.78	68.48 69.20 66.78	2.13×10^{-11} 1.92×10^{-11} 2.70×10^{-8}	2.13×10^{-11} 1.92×10^{-11} 2.70×10^{-8}	NA	NA
[53]	Illegal drugs	Topas	0.2–2 THz	81.41	NA	2.58×10^{-15}	NA	0.09835	NA
[64]	Water	Topas	0.5–1.5 THz	96.25	96.25	2.11×10^{-14}	2.11×10^{-14}	0.000916	0.000916
[69]	Water Ethanol Benzene	Zeonex	0.8–3 THz	84.25 86.32 88.36	84.25 86.32 88.36	5.55×10^{-10} 5.60×10^{-10} 6.60×10^{-10}	5.55×10^{-10} 5.60×10^{-10} 6.60×10^{-10}	0.00699	0.00699

Table 4. *Cont.*

Reference	Analyte	Background	Wavelength/Frequency	Sensitivity (%)		Confinement Loss (dB/cm)		EML (cm^{-1})	
				x-pol	*y*-pol	*x*-pol	*y*-pol	*x*-pol	*y*-pol
[70]	Glucose Plasma WBC RBC	Topas	1–4 THz	84.55 85.09 85.62 87.68	84.55 85.09 85.62 87.68	7.92×10^{-11} 6.66×10^{-11} 3.14×10^{-11} 1.86×10^{-11}	7.92×10^{-11} 6.66×10^{-11} 3.14×10^{-11} 1.86×10^{-11}	NA	NA
[71]	Camel milk Cow milk	Zeonex	0.2–2 THz	81.16 81.32	NA NA	8.675×10^{-18} 1.435×10^{-18}	NA NA	0.033013 0.03284	NA NA
[72]	Water Ethanol Benzene	Zeonex	1–2 THz	92.3 93.5 93.7	92.9 93.8 94.2	2.05×10^{-13} 8.48×10^{-13} 8.57×10^{-13}	1.61×10^{-13} 3.85×10^{-13} 1.28×10^{-13}	0.0058 0.0062 0.0064	0.0054 0.0057 0.0059
[73]	Chloropicrin Ethyl-bromide methyl-bromide	Zeonex	1–2 THz	94.6 92.7 93.3	94.5 92.5 93	8.34×10^{-13} 2.43×10^{-12} 4.70×10^{-12}	3.36×10^{-12} 1.27×10^{-12} 4.70×10^{-12}	0.009414 0.008116 0.008464	0.009095 0.007929 0.008243
[74]	NaCl	Zeonex	0.9–1.2 THz	91.5	91.7	NA	NA	0.0037	NA
[75]	Ethanol, Benzene Water	Topas	1–3 THz	86.5	86.5	6.67×10^{-8}	6.67×10^{-8}	NA	NA
[76]	Cocaine	Zeonex	0.4–1.6 THz	87.02	87.02	10^{-4}	10^{-4}	0.01	0.01
[77]	Alcohol	Topas	1–3 THz	88.7	88.7	5.75×10^{-8}	5.75×10^{-8}	NA	NA
[78]	Refractive index (1.364)	Topas	0.5–1.3 THz	89.7	89.7	2.18×10^{-12}	2.18×10^{-12}	NA	NA
[79]	Ethanol Benzene Water	Topas	0.6–1.6 THz	84.6	84.6	7.49×10^{-11}	7.49×10^{-11}	NA	NA
[80]	Formalin	Zeonex	1–2 THz	77.71	77.71	NA	NA	NA	NA
[81]	Ethanol Benzene Water	Topas	1.5–3.5 THz	79.99 80.27 79.39	79.99 80.27 79.39	1.18×10^{-12} 1.18×10^{-12} 1.18×10^{-12}	1.18×10^{-12} 1.18×10^{-12} 1.18×10^{-12}	NA	NA
[82]	Ethanol Benzene Water	Zeonex	1–3 THz	78.56 79.76 77.51	78.56 79.76 77.51	5.80×10^{-10} 6.02×10^{-10} 5.74×10^{-10}	5.80×10^{-10} 6.02×10^{-10} 5.74×10^{-10}	NA	NA

Table 4. *Cont.*

Reference	Analyte	Background	Wavelength/Frequency	Sensitivity (%)		Confinement Loss (dB/cm)		EML (cm^{-1})	
				x-pol	*y*-pol	*x*-pol	*y*-pol	*x*-pol	*y*-pol
[83]	Ethanol	Silica	0.8–2 μm	29.25	29.25	7.68×10^{-9}	7.68×10^{-9}	NA	NA
[84]	Benzene	Silica	0.8–1.5 μm	85.55	85.55	1.309×10^{-13}	1.309×10^{-13}	NA	NA
[85]	Gas	Silica	1.1–1.7 μm	75.14	75.14	1.41×10^{-4}	1.41×10^{-4}	NA	NA
[86]	Glucose Human mucosa	Silica	1.3–2 μm	47.59 47.31		6.54489×10^{-4}		NA	NA
[87]	Ammonia gas	Silica	1.544 μm	70.25		1.202×10^{-3}		NA	NA
Proposed Sensor	**Bilirubin**	**HRS**	**0.1–1.1 THz**	**95**	**98**	**2.64×10^{-15}**	**2.03×10^{-14}**	**0.00131**	**0.00193**

4. Conclusions

In this paper, a highly sensitive THz-PCF biosensor was numerically analyzed for measuring bilirubin concentrations in the blood. The HRS material was used to construct the suggested PCF sensor due to the fact of its index contrast relative to the bilirubin with a low absorption coefficient in the THz region. The numerical simulation results showed a high relative sensitivity of 95% and 98% for the x-polarized and y-polarized modes, respectively, at f = 0.75 THz. Moreover, the suggested THz-PCF donated a low confinement loss of 2.64×10^{-15} dB/cm for the x-polarized mode and 2.03×10^{-14} dB/cm for the y-polarized mode at f = 0.75 THz. Furthermore, a low EML of 0.00131 cm^{-1} was achieved for the x-polarized mode and 0.00193 cm^{-1} for the y-polarized mode. This sensor was aimed at helping in the effectively earlier detection of diseases that are based on the disruption of bilirubin concentrations in the blood; hence, it will help in health care.

Institutional Review Board Statement: Not applicable.

Informed Consent Statement: Not applicable.

Data Availability Statement: The data will be available upon request from the corresponding authors.

Conflicts of Interest: The authors declare no conflict of interest.

References

1. Tsuruda, K.; Fujita, M.; Nagatsuma, T. Extremely low-loss terahertz waveguide based on photonic crystal slab. *Opt. Express* **2015**, *23*, 31977–31990. [CrossRef] [PubMed]
2. Habib, A.; Anower, S.; Islam, N. Terahertz sensing based on photonic crystal fibers. In *Terahertz Technology*; You, B., Lu, J.U., Eds.; Intech Open: London, UK, 2021. [CrossRef]
3. Saadeldin, A.S.; Hameed, M.F.O.; Elkaramany, E.M.A.; Obayya, S.S.A. Highly Sensitive Terahertz Metamate-rial Sensor. *IEEE Sens. J.* **2019**, *19*, 7993–7999. [CrossRef]
4. Areed, N.F.F.; Fakharany, A.E.; Hameed, M.F.O.; Obayya, S.S.A. Controlled optical photonic crystal AND gate using nematic liquid crystal layers. *Opt Quant Electron.* **2017**, *49*, 45. [CrossRef]
5. Ibrahim, M.S.S.; El-Okr, M.M.; Hamed, M.K.G.; Obayya, S.S.A.; Hameed, M.F.O. Ultracompact tunable bifunctional XOR and XNOR photonic crystal logic gates. *Opt. Eng.* **2020**, *59*, 027106. [CrossRef]
6. Parandin, F.; Heidari, F.; Rahimi, Z.; Olyaee, S. Two-Dimensional photonic crystal Biosensors: A review. *Opt. Laser Technology.* **2021**, *144*, 107397. [CrossRef]
7. Parandin, F.; Heidari, F.; Aslinezhad, M.; Parandin, M.M.; Roshani, S.; Roshani, S. Design of 2D photonic crystal biosensor to detect blood components. *Opt Quant. Electron.* **2022**, *54*, 618. [CrossRef]
8. Olyaee, S.; Najafgholinezhad, S. A High Quality Factor and Wide Measurement Range Biosensor Based on Photonic Crystal Nanocavity Resonator. *Sens. Lett.* **2013**, *11*, 483–488. [CrossRef]
9. Ibrahim, M.S.S.; Hamed, M.K.G.; El-Okr, M.M.; Obayya, S.S.A.; Hameed, M.F.O. Highly sensitive photonic crystal gamma ray dosimeter. *Opt. Quantum Electron.* **2021**, *53*, 348. [CrossRef]
10. Ibrahim, M.S.S.; Tarek, M.; Obayya, S.S.A.; Hameed, M.F.O. Highly Sensitive 1D Photonic Crystal Biosensor. In Proceedings of the 2021 International Applied Computational Electromagnetics Society Symposium (ACES), Hamilton, ON, Canada, 1–5 August 2021.
11. Azzam, S.I.; Hameed, M.F.O.; Shehata, R.E.A.; Heikal, A.M.; Obayya, S.S.A. Multichannel photonic crystal fiber surface plasmon resonance-based sensor. *Opt. Quantum Electron.* **2016**, *48*, 142. [CrossRef]
12. *Fundamentals and Applications of Nanophotonics*, 1st ed.; Woodhead Publishing: Sawston, UK, 2016. [CrossRef]
13. Hossain, M.B.; Podder, E. Design and investigation of PCF-based blood components sensor in terahertz regime. *Appl. Phys. A* **2019**, *125*, 861. [CrossRef]
14. Rabeea, A.S.H.; Hameed, M.F.O.; Heikal, A.M.; Obayya, S.S.A. Highly sensitive photonic crystal fiber gas sen-sor. *Optik* **2019**, *188*, 78–86. [CrossRef]

15. Azab, M.Y.; Hameed, M.F.O.; El-Hefnawy, S.M.; Obayya, S.S.A. Ultra-compact liquid crystal dual core photonic crystal fibre multiplexer- demultiplexer. *IET Optoelectron.* **2015**, *10*, 21–27. [CrossRef]
16. Hameed, M.F.O.; Heikal, A.M.; Younis, B.M.; Abdelrazzak, M.; Obayya, S.S.A. Ultra-high tunable liquid crystal-plasmonic photonic crystal fiber polarization filter. *Opt. Express* **2015**, *23*, 7007–7020. [CrossRef] [PubMed]
17. Wei, L.; Yu, L.; Jiaoqi, H.; Guorong, H.; Yang, Z.; Weiling, F. Application of terahertz spectroscopy in biomolecule detection. *Front. Lab. Med.* **2018**, *2*, 127–133. [CrossRef]
18. Bulbul, A.A.M.; Rashed, A.N.Z.; El-Hageen, H.M.; Alatwi, A.M. Design and numerical analysis of an extremely sensitive PCF-based sensor for detecting kerosene adulteration in petrol and diesel. *Alex. Eng. J.* **2021**, *60*, 5419–5430. [CrossRef]
19. Ekhlasur Rahaman, M.; Bellal Hossain, M.; Shekhar Mondal, H.; Saha, R.; Mahbub Hossain, M.; Shamim Ahsan, M. Highly sensitive photonic crystal fiber liquid sensor in terahertz frequency range. *Mater. Today Proc.* **2020**, *43*, 3815–3820. [CrossRef]
20. Bulbul, A.A.M.; Jibon, R.H.; Biswas, S.; Pasha, S.T.; Sayeed, M.A. Photonic crystal fiber-based blood components detection in THz regime: Design and simulation. *Sens. Int.* **2021**, *2*, 100081. [CrossRef]
21. Islam, M.R.; Iftekher, A.N.M.; Mou, F.A.; Rahman, M.M.; Bhuiyan, M.I.H. Design of a Topas-based ultrahigh-sensitive PCF biosensor for blood component detection. *Appl. Phys. A* **2021**, *127*, 109. [CrossRef]
22. Ramachandran, A.; Babu, P.R.; Senthilnathan, K. Design of a terahertz chemical sensor using a dual steering-wheel microstructured photonic crystal fiber. *Photonics Nanostruct. Fundam. Appl.* **2021**, *46*, 100952. [CrossRef]
23. Jibon, R.H.; Ahmed, M.; Rahaman, M.E.; Hasan, M.K.; Shaikh, M.M.; Tooshil, A. Nicotine Sensing by Photonic Crystal Fiber in THz Regime. In Proceedings of the International Conference on Robotics, Electrical and Signal Processing Techniques, Dhaka, Bangladesh, 5–7 January 2021. [CrossRef]
24. Podder, E.; Hossain, M.B.; Ahmed, K. Photonic crystal fiber for milk sensing. *Sens. Bio.-Sens. Res.* **2022**, *38*, 100534. [CrossRef]
25. Porter, M.L.; Dennis, B.L. Hyperbilirubinemia in the term newborn. *Am. Fam. Phys.* **2022**, *65*, 599–606.
26. Rocher, S.P.; Kobos, R. Jaundice in the Adult Patient. *Am. Fam. Phys.* **2004**, *69*, 299–304.
27. Suh, S.; Cho, Y.R.; Park, M.K.; Kim, D.K.; Cho, N.H.; Lee, M.K. Relationship between serum bilirubin levels and cardiovascular disease. *PLoS ONE* **2018**, *13*, e0193041. [CrossRef] [PubMed]
28. Schieffer, K.M.; Bruffy, S.M.; Rauscher, R.; Koltun, W.A.; Yochum, G.S.; Gallagher, C.J. Reduced total serum bilirubin levels are associated with ulcerative colitis. *PLoS ONE* **2017**, *12*, e0179267. [CrossRef] [PubMed]
29. Wusthoff, C.J.; Loe, I.M. Impact of bilirubin-induced neurologic dysfunction on neurodevelopmental outcomes. *Semin. Fetal Neonatal Med.* **2017**, *176*, 139–148. [CrossRef] [PubMed]
30. Greco, C.; Arnolda, G.; Boo, N.Y.; Iskander, I.F.; Okolo, A.A.; Rohsiswatmo, R.; Coda Zabetta, C.D. Neonatal Jaundice in Low- and Middle-Income Countries: Lessons and Future Directions from the 2015 Don Ostrow Trieste Yellow Retreat. *Neonatology* **2016**, *110*, 172–180. [CrossRef]
31. Mostafa, M.A.; Kamal, N.M.; Eltaher, S.; Hamed, Y.; Abdelaziz, H.; Abdelghany, W.; Sherief, L.M. Knowledge of Neonatal Hyperbilirubinemia Among Primary Health Care Physicians: A Single-Center Experience. *Clin. Med. Insights Pediatr.* **2019**, *13*, 1179556518824375. [CrossRef]
32. El Meliegy, E.H.K.; El Sabbagh, M.H. Etiology of developmental delay in Egyptian children. *Int. J. Child Neuropsychiatr.* **2004**, *1*, 2919–2940.
33. Obayya, S.S.A. Efficient finite-element-based time-domain beam propagation analysis of optical integrated circuits. *IEEE J. Quantum Electron* **2004**, *40*, 591–595. [CrossRef]
34. *COMSOL Multiphysics 6.1*; COMSOL Inc.: Stockholm, Sweden, 2022. Available online: https://www.comsol.com (accessed on 1 January 2021).
35. Yang, T.; Ding, C.; Ziolkowski, R.W.; Guo, Y.J. A terahertz (THz) single-polarization-single-mode (SPSM) photonic crystal fiber (PCF). *Materials* **2019**, *12*, 2442. [CrossRef]
36. Dai, J.; Zhang, J.; Zhang, W.; Grischkowsky, D. Terahertz time-domain spectroscopy characterization of the far-infrared absorption and index of refraction of high-resistivity, float-zone silicon. *J. Opt. Soc. Am. B* **2004**, *21*, 1379. [CrossRef]
37. Zhang, T.; Demchenko, P.; Khodzitsky, M.K.; Kononova, Y.; Babenko, A.; Grineva, E. The Influence of Bilirubin and Creatinine on the Refractive Index of Whole Blood in Terahertz Frequency Range: A Qualitative Analysis. In Proceedings of the Optics in Health Care and Biomedical Optics VIII, Beijing, China, 23 October 2018. [CrossRef]
38. Chen, H.; Chen, X.; Ma, S.; Wu, X.; Yang, W.; Zhang, W.; Li, X. Quantify Glucose Level in Freshly Diabetic's Blood by Terahertz Time-Domain Spectroscopy. *J. Infrared Milli Terahz Waves* **2018**, *39*, 399–408. [CrossRef]
39. Bao, H.; Nielsen, K.; Rasmussen, H.K.; Jepsen, P.U.; Bang, O. Fabrication and characterization of porous-core honeycomb bandgap THz fibers. *Opt. Express* **2012**, *20*, 29507–29517. [CrossRef]
40. Katyba, G.M.; Zaytsev, K.I.; Chernomyrdin, N.V.; Shikunova, I.A.; Komandin, G.A.; Anzin, V.B.; Lebedev, S.P.; Spektor, I.E.; Karasik, V.E.; Yurchenko, S.O.; et al. Sapphire Photonic Crystal Waveguides for Terahertz Sensing in Aggressive Environments. *Adv. Opt. Mater.* **2018**, *6*, 1800573. [CrossRef]
41. Cordeiro, C.M.B.; Santos, E.M.D.; Cruz, C.H.B.; Matos, C.G.D.; Daniel, S.; Ferreira, D.S. Lateral access to the holes of photonic crystal fibers–selective filling and sensing applications. *Opt. Express* **2006**, *14*, 8403–8412. [CrossRef] [PubMed]
42. Islam, M.R.; Al Naser, A.M.; Jaba, F.Z.; Anzum, F.; Iftekher, A.N.M.; Khan, M.R.H.; Nishat, M.M. Design of a hexagonal outlined porous cladding with vacant core photonic crystal fibre biosensor for cyanide detection at THz regime. *IET Optoelectron.* **2022**, *13*, 160–173. [CrossRef]

43. Huang, Y.; Xua, Y.; Yariv, A. Fabrication of functional microstructured optical fibers through a selective-filling technique. *Appl. Phys. Lett.* **2004**, *85*, 5182–5184. [CrossRef]

44. Kuo, S.M.; Huang, Y.W.; Yeh, S.M.; Cheng, W.H.; Lin, C.H. Liquid Crystal Modified Photonic Crystal Fiber (LC-PCF) Fabricated with an SU-8 Photoresist Sealing Technique for Electrical Flux Measurement. In Proceedings of the 2010 IEEE 23rd International Conference on Micro Electro Mechanical Systems (MEMS), Hong Kong, China, 24–28 January 2010. [CrossRef]

45. Bowden, B.; Harrington, J.A.; Mitrofanov, O. Silver/Polystyrene-coated hollow glass waveguides for the transmission of terahertz radiation. *Opt. Lett.* **2007**, *32*, 2945–2947. [CrossRef]

46. Salamin, Y.; Chelmus, I.C.; Fedoryshyn, Y.; Heni, W.; Elder, D.L.; Dalton, L.R.; Faist, J.; Leuthold, J. Compact and ultra-efficient broadband plasmonic terahertz field detector. *Nat. Commun.* **2009**, *10*, 5550. [CrossRef]

47. Rahman, B.M.A.; Agrawal, A. *Finite Element Modeling Methods for Photonics*, 1st ed.; Artech House: Boston, MA, USA, 2013.

48. Obayya, S.S.A.; Azizur Rahman, B.M.; El-Mikati, H.A. New Full-Vectorial Numerically Efficient Propagation Algorithm Based on the Finite Element Method. *J. Light. Technol.* **2000**, *18*, 409–415. [CrossRef]

49. Islam, A.; Rakibul, M.; Ahmed, I.; Al, M.; Fariha, N.; Fatema, A.; Jaba, Z. Square structured photonic crystal fiber based THz sensor design for human body protein detection. *J. Comput Electron.* **2020**, *20*, 377–386. [CrossRef]

50. Sultana, J.; Islam, S.; Faisal, M.; Rakibul, M.; Ng, B.W.; Ebendorff-heidepriem, H.; Abbott, D. Highly birefringent elliptical core photonic crystal fiber for terahertz application. *Opt. Commun.* **2018**, *407*, 92–96. [CrossRef]

51. Mou, F.A.; Rahman, M.M.; Islam, M.R.; Bhuiyan, M.I.H. Development of a photonic crystal fiber for THz wave guidance and environmental pollutants detection. *Sens. Bio-Sens. Res.* **2020**, *29*, 100346. [CrossRef]

52. Habib, A.; Anower, S.; Abdulrazak, L.F.; Reza, S. Hollow core photonic crystal fiber for chemical identification in terahertz regime. *Opt. Fiber Technol.* **2019**, *52*, 101933. [CrossRef]

53. Tahhan, S.R.; Aljobouri, H.K. Sensing of Illegal Drugs by Using Photonic Crystal Fiber in Terahertz Regime. *J. Opt. Commun.* **2020**. [CrossRef]

54. Hasanuzzaman, G.K.M.; Rana, S.; Habib, S. A Novel Low Loss, Highly Birefringent Photonic Crystal Fiber in THz Regime. *IEEE Photonics Technol. Lett.* **2016**, *28*, 899–902. [CrossRef]

55. Liang, J.; Ren, L.; Chen, N.; Zhou, C. Broadband, low-loss, dispersion flattened porous-core photonic bandgap fiber for terahertz (THz)-wave propagation. *Opt. Commun.* **2013**, *295*, 257–261. [CrossRef]

56. Habib, A.; Anower, S.; Haque, I. Highly sensitive hollow core spiral fiber for chemical spectroscopic applications. *Sens. Int.* **2020**, *1*, 100011. [CrossRef]

57. Arif, M.F.H.; Ahmed, K.; Asaduzzaman, S.; Azad, M. Design and optimization of photonic crystal fiber for liquid sensing applications. *Photonic Sens.* **2016**, *6*, 279–288. [CrossRef]

58. Hossain, B.; Podder, E.; Bulbul, A.A.; Mondal, H.S. Optical Fiber Technology Bane chemicals detection through photonic crystal fiber in THz regime. *Opt. Fiber Technol.* **2020**, *54*, 102102. [CrossRef]

59. Hossain, M.S.; Sen, S.; Hossain, M.M. Design of a chemical sensing circular photonic crystal fiber with high relative sensitivity and low confinement loss for terahertz (THz) regime. *Optik.* **2020**, *222*, 165359. [CrossRef]

60. Rahman, M.M.; Mou, F.A.; Bhuiyan, M.I.H.; Islam, M.R. Refractometric THz Sensing of Blood Components in a Photonic Crystal Fiber Platform. *Braz. J. Phys.* **2022**, *52*, 47. [CrossRef]

61. Podder, E.; Hossain, B.; Rahaman, E.; Bulbul, A.A.; Ahmed, K. Ensing and Bio-Sensing Research Design and optimization of terahertz blood components sensor using photonic crystal fiber. *Sens. Bio.-Sens. Res.* **2020**, *30*, 100386. [CrossRef]

62. Habib, M.A.; Vera, E.R.; Aristizabal, J.V.; Anower, M.S. Numerical Modeling of a Rectangular Hollow-Core Waveguide for the Detection of Fuel Adulteration in Terahertz Region. *Fibers* **2020**, *8*, 63. [CrossRef]

63. Jibon, R.H.; Biswas, S.; Nira, N.F.I. Poisonous chemical detection in the THz regime using PCF: Design and numerical investigation. *J. Opt.* **2021**, *50*, 671–680. [CrossRef]

64. Hossain, M.S.; Sen, S. Design and Performance Improvement of Optical Chemical Sensor Based Photonic Crystal Fiber (PCF) in the Terahertz (THz) Wave Propagation. *Silicon* **2020**, *13*, 3879–3887. [CrossRef]

65. Sultana, J.; Islam, M.S.; Dinovitser, A.; Brian, W.-H.N.; Abbott, D. A novel Zeonex based oligoporous-core photonic crystal fiber for polarization preserving terahertz applications. *Opt. Commun.* **2018**, *413*, 242–248. [CrossRef]

66. Ultana, J.A.S.; Slam, M.D.S.A.I. Terahertz detection of alcohol using a photonic crystal fiber sensor. *Appl. Opt.* **2018**, *57*, 2426–2433. [CrossRef] [PubMed]

67. Cordeiro, C.M.D.; Ng, A.K.L.; Heidepriem, H. E.Ultrasimplifed Single-Step Fabrication of Microstructured Optical Fiber. *Sci. Rep.* **2020**, *10*, 9678. [CrossRef] [PubMed]

68. Rahaman, M.E.; Jibon, R.H.; Mondal, H.S.; Hossain, M.B.; Bulbul, A.A.M.; Saha, R. Design and optimization of a PCF-based chemical sensor in THz regime. *Sens. Bio-Sens. Res.* **2021**, *32*, 100422. [CrossRef]

69. Hossain, M.S.; Kamruzzaman, M.M.; Sen, S.; Azad, M.M.; Hossain Mollah, M.S. Hexahedron core with sensor based photonic crystal fiber: An approach of design and performance analysis. *Sens. Bio-Sens. Res.* **2021**, *32*, 100426. [CrossRef]

70. Kumar, A.; Verma, P.; Jindal, P. Decagonal solid core PCF based refractive index sensor for blood cells detection in terahertz regime. *Opt. Quantum Electron* **2021**, *53*, 165. [CrossRef]

71. Islam, M.A.; Islam, M.R.; Siraz, S.; Rahman, M.; Anzum, M.S.; Noor, F. Wheel structured Zeonex-based photonic crystal fiber sensor in THz regime for sensing milk. *Appl. Phys. A* **2021**, *127*, 311. [CrossRef] [PubMed]

72. Jibon, R.H.; Rahaman, M.K.; Alahe, M.A. Detection of primary chemical analytes in the THz regime with photonic crystal fiber. *Sens. Bio-Sens. Res.* **2021**, *33*, 100427. [CrossRef]

73. Jibon, R.H.; Ahmed, M.; Abd-Elnaby, M.; Rashed, A.N.Z.; Eid, M.M.A. Design mechanism and performance evaluation of photonic crystal fiber (PCF)-based sensor in the THz regime for sensing noxious chemical substrates of poultry feed. *Appl. Phys. A* **2022**, *128*, 169. [CrossRef]

74. Bulbul, A.A.M.; Hossain, M.B.; Dutta, R.; Hassan, M. Zeonex-based Tetra-rectangular Core-photonic Crystal Fiber for NaCl Detection. *Nanosci. Nanotechnol. Asia* **2021**, *11*, 112–120. [CrossRef]

75. Hossain, M.S.; Faruq, M.A.; Rana, M.M.; Sen, S.; Haque, M.D.; Azad, M.M. Sensitivity analysis for detecting chemi-cals by the optical chemical sensor based Photonic Crystal Fiber (PCF) in the Terahertz (THz) regime. *Phys Scr.* **2021**, *96*, 125121. [CrossRef]

76. Suhaimi, N.A.N.B.; Yakasai, I.K.; Abas, E.; Kaijage, S.; Begum, F. Modelling and simulation of novel liquid-infiltrated PCF biosensor in Terahertz frequencies. *IET Optoelectron.* **2020**, *14*, 411–416. [CrossRef]

77. Hossain, M.S.; Hussain, N.; Hossain, Z.; Zaman, M.S.; Rangon, M.N.H.; Al-Shafi, M.A.; Sen, S.; Azad, M.M. Performance analysis of alcohols sensing with optical sensor procedure using circular photonic crystal fiber (C-PCF) in the terahertz regime. *Sens. Bio-Sens. Res.* **2022**, *35*, 100469. [CrossRef]

78. Luo, W.; Jiang, P.; Xu, Q.; Cao, L.; Jones, A.; Li, K.; Copner, N.; Gong, Y. Terahertz Sensor via Ultralow-Loss Dispersion-Flattened Polymer Optical Fiber: Design and Analysis. *Materials* **2021**, *14*, 4921. [CrossRef]

79. Lu Xue, L.; Yani, Z.; Yuyu, Z. Terahertz Detection of Chemical Analytes Using a Hollow-Core Photonic Crystal Fiber Sensor. In Proceedings of the 2019 International Conference on Optical Instruments and Technology: IRMMW-THz Technologies and Applications, Beijing, China, 12 March 2020. [CrossRef]

80. Bulbul, A.A.M.; Jibon, R.H.; Das, S.K.; Roy, T.; Saha, A.; Hossain, M.B. PCF Based Formalin Detection by Exploring the Optical Properties in THz Regime. *Nanosci. Nanotechnol. Asia* **2020**, *11*, 314–321. [CrossRef]

81. Ahmed, K.; Paul, B.K.; Ahmed, F.; Jabin, M.A.; Uddin, M.S. Numerical demonstration of triangular shaped photonic crystal fibre-based biosensor in the Terahertz range. *IET. Opt. Electron.* **2021**, *15*, 1. [CrossRef]

82. Sen, S.; Al-Shafi, A.; Sikder, A.S.; Hossain, S.; Azad, M.M. Zeonex based decagonal photonic crystal fiber (D-PCF) in the terahertz (THz) band for chemical sensing applications. *Sens. Bio-Sens. Res.* **2021**, *31*, 100393. [CrossRef]

83. Asaduzzaman, S.; Ahmed, K. Microarray-core based circular photonic crystal fiber for high chemical sensing capacity with low confinement loss. *Opt. Appl.* **2017**, *47*, 41–49. [CrossRef]

84. Anik, H.K.; Mahmud, S.; Chakma, P.; Talukder, H.; Chakrabarti, K.; Biswa, S.K. A Highly Sensitive and Ultra-Low Loss Photonic Crystal Fiber-Based Gas and Chemical Sensor. In *Proceedings of the 3rd International Conference on Communication, Devices and Computing*, 1st ed.; Skdar, B., Maity, S.P., Samanta, J., Roy, A., Eds.; Springer: Singapore, 2021; Volume 851, pp. 33–34.

85. Abbaszadeh, A.; Makouei, S.; Meshgini, S. Highly sensitive triangular photonic crystal fiber sensor design applicable for gas detection. *Adv. Electromagn.* **2021**, *10*, 1–5. [CrossRef]

86. Leon, M.J.B.M.; Abedin, S.; Kabir, M.A. A photonic crystal fiber for liquid sensing application with high sensitivity, birefringence and low confinement loss. *Sens. Int.* **2021**, *2*, 100061. [CrossRef]

87. Abbaszadeh, A.; Makouei, S.; Meshgini, S. New hybrid photonic crystal fiber gas sensor with high sensitivity for ammonia gas detection. *Can. J. Phys.* **2022**, *100*, 129–137. [CrossRef]

88. Doumas, B.T.; Perry, B.W.; Sasse, E.A.; Straumfjord, J.V. Standardization in Bilirubin Assays: Evaluation of Selected Methods and Stability of Bilirubin Solutions. *Clin. Chem.* **1973**, *19*, 984–993. [CrossRef]

89. Li, X.; Rosenzweig, Z. A fiber optic sensor for rapid analysis of bilirubin in serum. *Anal. Chim. Acta* **1997**, *353*, 263–273. [CrossRef]

90. Bergmeyer, H.U.; Horder, M.; Rej, R. Approved recommendations on IFCC methods of measurement of catalytic concentration of enzymes. *J. Clin. Chem. Clin. Biochem.* **1986**, *24*, 481–489.

91. Jayasree, M.; Aparna, R.S.; Anjana, R.R.; Devi, J.S.A.; John, N.; Abha, K.; Manikandan, A.; George, S. Fluorescence turn on detection of bilirubin using Fe (III) modulated BSA stabilized copper nanocluster; A mechanistic perception. *Anal. Chim. Acta* **2018**, *1031*, 152–160. [CrossRef] [PubMed]

92. Narwal, V.; Batra, B.; Kalra, V.; Jalandra, R.; Ahlawat, J.; Hooda, R.; Sharma, M.; Rana, J.S. Bilirubin detection by different methods with special emphasis on biosensing: A review. *Sens. Bio-Sens. Res.* **2021**, *33*, 100436. [CrossRef]

93. Thangamuthu, M.; Gabriel, W.E.; Santschi, C.; Martin, O.J.F. Electrochemical Sensor for Bilirubin Detection Using Screen Printed Electrodes Functionalized with Carbon Nanotubes and Graphene. *Sensors* **2018**, *18*, 800. [CrossRef] [PubMed]

94. Mohamad, M.; Manap, H. The optimal absorption of bilirubin using an optical fiber sensor. *ARPN J. Eng. Appl. Sci.* **2015**, *10*, 8762–8764.

95. Guo, Z.; Zhang, T.; Song, J.; Jiang, H.; Chen, H. Sensitivity of topological edge states in a non-Hermitian dimer chain. *Photonics Res.* **2021**, *9*, 574–582. [CrossRef]

96. Gabrys, P.A.; Seo, S.E.; Wang, M.X.; Oh, E.; Macfarlane, R.J.; Mirkin, C.A. Lattice Mismatch in Crystalline Nanoparticle Thin Films. *Nano Lett.* **2018**, *18*, 579–585. [CrossRef]

97. Guo, Z.; Long, Y.; Jiang, H.; Ren, J.; Chen, H. Anomalous unidirectional excitation of high-k hyperbolic modes using all-electric metasources. *Adv. Photonics* **2021**, *3*, 360011–3600110. [CrossRef]
98. Hu, S.; Chen, Y.; Chen, L.; Zheng, H.; Azeman, N.H.; Liu, M.X.; Liu, G.S.; Luo, Y.; Chen, Z. High-performance fiber plasmonic sensor by engineering the dispersion of hyperbolic metamaterials composed of Ag/TiO$_2$. *Opt. Express* **2020**, *28*, 25562–25573. [CrossRef]